

Characterization of optical properties of ZnO nanoparticles for quantitative imaging of transdermal transport

Zhen Song,¹ Timothy A. Kelf,¹ Washington H. Sanchez,² Michael S. Roberts,^{2,4}
Jaro Rička,³ Martin Frenz,³ and Andrei V. Zvyagin^{1,*}

¹*MQ Biofocus Research Centre, Macquarie University, Sydney, NSW 2109, Australia*

²*Therapeutics Research Centre, School of Medicine, The University of Queensland, Brisbane, QLD 4102, Australia*

³*Institute of Applied Physics, University of Bern, Sidlerstrasse 5, CH-3012 Bern, Switzerland*

⁴*School of Pharmacy & Medical Sciences, University of South Australia, Adelaide, 5001, Australia*

*andrei.zvyagin@mq.edu.au

Abstract: Widespread applications of ZnO nanoparticles (NP) in sun-blocking cosmetic products have raised safety concerns related to their potential transdermal penetration and resultant cytotoxicity. Nonlinear optical microscopy provides means for high-contrast imaging of ZnO NPs lending *in vitro* and *in vivo* assessment of the nanoparticle uptake in skin, provided their nonlinear optical properties are characterized. We report on this characterization using ZnO NP commercial product, Zinclear, mean-sized 21 nm. Two-photon action cross-section of this bandgap material ($E_{\text{bg}} = 3.37$ eV, $\lambda_{\text{bg}} = 370$ nm) measured by two techniques yielded consistent results of $\eta_{\text{ZnO}} \sigma_{\text{ZnO}}^{(2\text{ph})} = 6.2 \pm 0.8$ μGM at 795 nm, and 32 ± 6 μGM at 770 nm per unit ZnO crystal cell, with the quantum efficiency of $\eta_{\text{ZnO}} = (0.9 \pm 0.2)$ %. In order to demonstrate the quantitative imaging, nonlinear optical microscopy images of the excised human skin topically treated with Zinclear were acquired and processed using $\sigma_{\text{ZnO}}^{(2\text{ph})}$ and η_{ZnO} values yielding nanoparticle concentration map in skin. Accumulations of Zinclear ZnO nanoparticles were detected only on the skin surface and in skin folds reaching concentrations of 800 NPs per μm^3 .

© 2011 Optical Society of America

OCIS codes: (160.2540) Fluorescent and luminescent materials; (160.4236) Nanomaterials; (170.3880) Medical and biological imaging; (180.4315) Nonlinear microscopy; (250.5230) Photoluminescence

References and links

1. Z. K. Tang, G. K. L. Wong, P. Yu, M. Kawasaki, A. Ohtomo, H. Koinuma, and Y. Segawa, "Room-temperature ultraviolet laser emission from self-assembled ZnO microcrystallite thin films," *Appl. Phys. Lett.* **72**(25), 3270–3272 (1998).
2. S. E. Cross, B. Innes, M. S. Roberts, T. Tsuzuki, T. A. Robertson, and P. McCormick, "Human skin penetration of sunscreen nanoparticles: in-vitro assessment of a novel micronized zinc oxide formulation," *Skin Pharmacol. Physiol.* **20**(3), 148–154 (2007).
3. F. Pflücker, V. Wendel, H. Hohenberg, E. Gärtner, T. Will, S. Pfeiffer, R. Wepf, and H. Gers-Barlag, "The human stratum corneum layer: an effective barrier against dermal uptake of different forms of topically applied micronised titanium dioxide," *Skin Pharmacol. Appl. Skin Physiol.* **14**(Suppl 1), 92–97 (2001).
4. Zs. Kertesz, Z. Szikszai, and A. Z. Kiss, "Quality of skin as a barrier to ultra-fine particles. Contribution of the IBA Group to the Nanoderm EU-5 Project in 2003-2004," in *ATOMKI Annual Report 2004* (Institute of Nuclear Research of the Hungarian Academy of Sciences, 2005), p. 70.
5. T. Xia, M. Kovochich, M. Liong, L. Mädler, B. Gilbert, H. B. Shi, J. I. Yeh, J. I. Zink, and A. E. Nel, "Comparison of the mechanism of toxicity of zinc oxide and cerium oxide nanoparticles based on dissolution and oxidative stress properties," *ACS Nano* **2**(10), 2121–2134 (2008).
6. Y. B. Zhang, W. Chen, S. P. Wang, Y. F. Liu, and C. Pope, "Phototoxicity of zinc oxide nanoparticle conjugates in human ovarian cancer NIH: OVCAR-3 cells," *J. Biomed. Nanotechnol.* **4**(4), 432–438 (2008).

7. C. G. J. Hayden, S. E. Cross, C. Anderson, N. A. Saunders, and M. S. Roberts, "Sunscreen penetration of human skin and related keratinocyte toxicity after topical application," *Skin Pharmacol. Physiol.* **18**(4), 170–174 (2005).
8. B. C. Heng, X. X. Zhao, S. J. Xiong, K. W. Ng, F. Y.-C. Boey, and J. S.-C. Loo, "Toxicity of zinc oxide (ZnO) nanoparticles on human bronchial epithelial cells (BEAS-2B) is accentuated by oxidative stress," *Food Chem. Toxicol.* **48**(6), 1762–1766 (2010).
9. C. Hanley, A. Thurber, C. Hanna, A. Punnoose, J. H. Zhang, and D. G. Wingett, "The Influences of Cell Type and ZnO Nanoparticle Size on Immune Cell Cytotoxicity and Cytokine Induction," *Nanoscale Res. Lett.* **4**(12), 1409–1420 (2009).
10. A. V. Zvyagin, X. Zhao, A. Gierden, W. H. Sanchez, J. A. Ross, and M. S. Roberts, "Imaging of zinc oxide nanoparticle penetration in human skin in vitro and in vivo," *J. Biomed. Opt.* **13**(6), 064031 (2008).
11. M. J. Osmond and M. J. McCall, "Zinc oxide nanoparticles in modern sunscreens: an analysis of potential exposure and hazard," *Nanotoxicology* **4**(1), 15–41 (2010).
12. M. S. Roberts, M. J. Roberts, T. A. Robertson, W. Sanchez, C. Thörling, Y. Zou, X. Zhao, W. Becker, and A. V. Zvyagin, "In vitro and in vivo imaging of xenobiotic transport in human skin and in the rat liver," *J. Biophotonics* **1**(6), 478–493 (2008).
13. A. P. Popov, A. V. Zvyagin, J. Lademann, M. S. Roberts, W. Sanchez, A. V. Priezzhev, and R. Myllylä, "Designing inorganic light-protective skin nanotechnology products," *J. Biomed. Nanotechnol.* **6**(5), 432–451 (2010).
14. L. L. Lin, J. E. Grice, M. K. Butler, A. V. Zvyagin, W. Becker, T. A. Robertson, H. P. Soyer, M. S. Roberts, and T. W. Prow, "Time-correlated single photon counting for simultaneous monitoring of zinc oxide nanoparticles and NAD(P)H in intact and barrier-disrupted volunteer skin," *Pharm. Res.* **28**(11), 2920–2930 (2011).
15. B. Gulson, M. McCall, M. Korsch, L. Gomez, P. Casey, Y. Oytam, A. Taylor, M. McCulloch, J. Trotter, L. Kinsley, and G. Greenoak, "Small amounts of zinc from zinc oxide particles in sunscreens applied outdoors are absorbed through human skin," *Toxicol. Sci.* **118**(1), 140–149 (2010).
16. B. Nanda and R. S. R. Murthy, "Preparation and characterization of chitosan lactate nanoparticles for the nasal delivery of enalaprilat," *J. Biomed. Nanotech.* **3**(1), 45–51 (2007).
17. A. P. Popov, J. Lademann, A. V. Priezzhev, and R. Myllylä, "Effect of size of TiO₂ nanoparticles embedded into stratum corneum on ultraviolet-A and ultraviolet-B sun-blocking properties of the skin," *J. Biomed. Opt.* **10**(6), 064037 (2005).
18. J. Lademann, H. J. Weigmann, C. Rickmeyer, H. Barthelmes, H. Schaefer, G. Mueller, and W. Sterry, "Penetration of titanium dioxide microparticles in a sunscreen formulation into the horny layer and the follicular orifice," *Skin Pharmacol. Appl. Skin Physiol.* **12**(5), 247–256 (1999).
19. B. R. Masters and P. T. C. So, "Confocal microscopy and multi-photon excitation microscopy of human skin in vivo," *Opt. Express* **8**(1), 2–10 (2001).
20. R. M. Williams, A. Flesken-Nikitin, A. Y. Nikitin, and W. R. Zipfel, "Multiphoton microscopy of intrinsic tissue emissions for cancer research," *FASEB J.* **21**, A601 (2007).
21. W. R. Zipfel, R. M. Williams, and W. W. Webb, "Nonlinear magic: multiphoton microscopy in the biosciences," *Nat. Biotechnol.* **21**(11), 1369–1377 (2003).
22. B. R. Masters and P. T. C. So, "Multi-photon excitation microscopy and confocal microscopy imaging of in vivo human skin: A comparison," *Microsc. Microanal.* **5**(4), 282–289 (1999).
23. J. A. Palero, H. S. de Bruijn, A. van der Ploeg van den Heuvel, H. J. Sterenborg, and H. C. Gerritsen, "Spectrally resolved multiphoton imaging of in vivo and excised mouse skin tissues," *Biophys. J.* **93**(3), 992–1007 (2007).
24. D. C. Dai, S. J. Xu, S. L. Shi, M. H. Xie, and C. M. Che, "Efficient multiphoton-absorption-induced luminescence in single-crystalline ZnO at room temperature," *Opt. Lett.* **30**(24), 3377–3379 (2005).
25. Z.-W. Dong, C.-F. Zhang, G.-J. You, X.-Q. Qiu, K.-J. Liu, Y.-L. Yan, and S.-X. Qian, "Multi-photon excitation UV emission by femtosecond pulses and nonlinearity in ZnO single crystal," *J. Phys. Condens. Matter* **19**(21), 216202 (2007).
26. X. J. Zhang, W. Ji, and S. H. Tang, "Determination of optical nonlinearities and carrier lifetime in ZnO," *J. Opt. Soc. Am. B* **14**(8), 1951–1955 (1997).
27. S. K. Das, M. Biswas, D. Byrne, M. Bock, E. McGlynn, M. Breusing, and R. Grunwald, "Multiphoton-absorption induced ultraviolet luminescence of ZnO nanorods using low-energy femtosecond pulses," *J. Appl. Phys.* **108**(4), 043107–043112 (2010).
28. C. Y. Liu, B. P. Zhang, N. T. Binh, and Y. Segawa, "Second harmonic generation in ZnO thin films fabricated by metalorganic chemical vapor deposition," *Opt. Commun.* **237**(1-3), 65–70 (2004).
29. L. Guo, S. H. Yang, C. L. Yang, P. Yu, J. N. Wang, W. K. Ge, and G. K. L. Wong, "Highly monodisperse polymer-capped ZnO nanoparticles: Preparation and optical properties," *Appl. Phys. Lett.* **76**(20), 2901–2903 (2000).
30. L. Irimpan, V. P. N. Nampoori, P. Radhakrishnan, B. Krishnan, and A. Deepthy, "Size-dependent enhancement of nonlinear optical properties in nanocolloids of ZnO," *J. Appl. Phys.* **103**(3), 033105 (2008).
31. L. Irimpan, A. Deepthy, B. Krishnan, L. M. Kukreja, V. P. N. Nampoori, and P. Radhakrishnan, "Effect of self assembly on the nonlinear optical characteristics of ZnO thin films," *Opt. Commun.* **281**(10), 2938–2943 (2008).
32. M. H. Majles Ara, Z. Dehghani, and S. Saievar Iranizad, "Synthesis, characterization and single-beam Z-scan measurement of the third-order optical nonlinearities of ZnO nano-particles," *Int. J. Mod. Phys. B* **22**(18 & 19), 3165–3171 (2008).

33. M. G. Vivas, T. Shih, T. Voss, E. Mazur, and C. R. Mendonca, "Nonlinear spectra of ZnO: reverse saturable, two- and three-photon absorption," *Opt. Express* **18**(9), 9628–9633 (2010).
34. J. H. Lin, Y. J. Chen, H. Y. Lin, and W. F. Hsieh, "Two-photon resonance assisted huge nonlinear refraction and absorption in ZnO thin films," *J. Appl. Phys.* **97**(3), 033526 (2005).
35. T. Tsuzuki and P. G. McCormick, "ZnO nanoparticles synthesised by mechanochemical processing," *Scr. Mater.* **44**(8-9), 1731–1734 (2001).
36. M. Kauert, P. C. Stoller, M. Frenz, and J. Růčka, "Absolute measurement of molecular two-photon absorption cross-sections using a fluorescence saturation technique," *Opt. Express* **14**(18), 8434–8447 (2006).
37. M. Schubnell, I. Kamber, and P. Beaud, "Photochemistry at high temperatures - Potential of ZnO as a high temperature photocatalyst," *Appl. Phys., A Mater. Sci. Process.* **64**(1), 109–113 (1997).
38. T. M. Stachelek, T. A. Pazoha, W. M. McClain, and R. P. Drucker, "Detection and assignment of the "phantom" photochemical singlet of trans-stilbene by two-photon excitation," *J. Chem. Phys.* **66**(10), 4540–4543 (1977).
39. M. A. Albota, C. Xu, and W. W. Webb, "Two-photon fluorescence excitation cross sections of biomolecular probes from 690 to 960 nm," *Appl. Opt.* **37**(31), 7352–7356 (1998).
40. W. R. Zipfel, R. M. Williams, R. Christie, A. Y. Nikitin, B. T. Hyman, and W. W. Webb, "Live tissue intrinsic emission microscopy using multiphoton-excited native fluorescence and second harmonic generation," *Proc. Natl. Acad. Sci. U.S.A.* **100**(12), 7075–7080 (2003).

1. Introduction

ZnO nanomaterial affords a range of important applications due to its unique optical properties. The bulk properties of a wide direct band gap (3.37 eV at room temperature) and high exciton binding energy (60 meV) are appealing for a new generation ultraviolet (UV) optoelectronics, including light-emitting diodes, diode lasers and field emission displays. High third-order nonlinearity of ZnO attracts researchers toward development of prospective optical devices, such as optical switches and optical phase conjugators [1]. In addition, the high optical absorption of ZnO in both UVA (spectral ranges 400 nm to 315 nm) and UVB (315 nm to 280 nm) is widely utilized in cosmetics for UV screening to protect against the radiation damage of skin. The use of ZnO nanoparticles (NP) in modern sunscreen formulations allows uniform coverage of skin surface, and renders sunscreen transparent improving overall aesthetic appeal. The cosmetic industry push toward further improvements in sunscreen transparency leads to reduction of ZnO particles mean-size below 20 nm, although this is tempered by the safety concerns associated with ZnO NP penetration in skin [2]. Application of ZnO-based sunscreen is generally regarded safe, if the nanomaterial stays on the skin surface, or is confined in *stratum corneum* (SC), the uppermost layer of skin. Despite SC is only about 10-40 μm thick (with a notable exception of palms of hands and soles of feet), it provides superb protection against environmental assault, which is due to its material-tight structure comprised dried flattened cells, corneocytes, cemented together by a lipid bilayer [3,4]. The next underlying skin layer, termed viable epidermis, contains viable cells, which are susceptible to toxicological hazards associated with extraneous nanomaterials. The toxicological risks of ZnO nanomaterial in viable epidermis is hotly debated, whereas cytotoxic effects of ZnO NP have been proven in epithelial cells, neural stem cells and various types of immune cells [5–9]. It is, therefore, consented that it is best to avoid penetration of ZnO NPs into viable epidermis and deeper skin layers. Hence, assessment of ZnO NP concentration in skin, including SC, viable epidermis and deeper dermal layers of skin becomes an important research focus in cosmetics, dermatology, and nanotoxicology [2,7,10–14].

A number of techniques have been demonstrated for assaying of skin nanomaterial absorption in skin. Among these, radiolabelling, cathodoluminescence and Franz cell assaying [15,16]. These techniques are, however, limited to *in vitro* studies. Electron microscopy/spectroscopy methods provide detailed morphological information at the nanometer-scale, but suffer from potential distortion of the skin transport properties. Besides, the associated skin preparation procedure is tedious and costly. Analysis of the NP distribution in SC by tape stripping methods have been demonstrated to be reasonably accurate assaying of metal oxide nanoparticle distribution in skin layers, although being

essentially non-local and invasive [17,18]. In comparison with the existing methods of the analysis of nanoparticle distribution in skin, nonlinear optical microscopy (NLOM) has demonstrated a considerable promise, as an *in vivo* imaging modality capable of providing clear images of the subsurface skin layers (at a depth of $\leq 200\ \mu\text{m}$ in turbid biological tissue) at the sub-cellular resolution [19–21]. In particular, NLOM imaging has revealed *in vivo* that topically applied ZnO NPs mean-sized $\sim 20\ \text{nm}$ stayed in SC and accumulated in skin folds and hair follicles [10]. ZnO NP appeared to exhibit high NLOM-imaging contrast on the intense autofluorescence background of live skin. Partly, it was due to the excitation wavelength, 740 nm, at which the imaging penetration depth was maximized, as the tissue scattering and absorption were minimized [22]; and also due to the emission wavelength at 385 nm, where the two-photon-excited skin tissue autofluorescence was relatively low [23]. Quantitative evaluation of the ZnO-nano distribution in skin, however, remains a challenge due to the non-reproducible laser excitation conditions, such as the pulse width variation, and variable nonlinear properties of ZnO nanomaterial. This challenge is addressed in this paper.

Ample literature is devoted to characterization of nonlinear optical properties of ZnO bulk [24–26], and, recently, ZnO nanomaterials, which are mainly governed by the 2nd- [$\chi^{(2)}$] and 3rd- [$\chi^{(3)}$] order electric susceptibilities. $\chi^{(2)}$ is responsible for the second-harmonic generation (SHG) processes in ZnO bulk and nanomaterials [27,28], whereas the imaginary part of $\chi^{(3)}$ governs the two-photon-absorption-induced photoluminescence (TPIL). Although $\text{Im}[\chi^{(3)}]$ does not capture the full spectral content of ZnO photoluminescence (PL), due to the effects of impurity-induced energy states in the bandgap, it lends an initial interpretation of TPIL principle UV spectral band emission centered at 385 nm. At the nanoscale, ZnO properties are found to deviate from these of bulk. The quantum confinement effects result in a blue-shift of the absorption and emission bands of ZnO NP of diameters $< 5\ \text{nm}$, and also account for the emission enhancement [29]. At the same time, the quantum effects alone fail to explain an approximately hundred-fold emission enhancement in case of ZnO NP of diameter $> 10\ \text{nm}$, invoking impurity- or surface- mediated excitation processes, whose mechanisms are still under research highlight [30]. TPIL is of prime interest in the NLOM imaging of ZnO NP, with an SHG contribution at the smaller scale. It is important to note that the use of $\text{Im}[\chi^{(3)}]$ is not favored by the biomedical optics convention that gives preference to a linearly-related quantity of a two-photon action cross-section, $\eta_{\text{ZnO}}\sigma_{\text{ZnO}}^{(2ph)}$ defined as a product of the quantum efficiency, η_{ZnO} (a ratio of emitted to absorbed photon energies) and the two-photon absorption cross-section, $\sigma_{\text{ZnO}}^{(2ph)}$.

Among several techniques used for determination of the two-photon absorption cross-section, Z-scan is most popular and conceptually straightforward [31–33]. In brief, a focused (short-pulse) probe beam is axially scanned through a sample eliciting two types of nonlinear optical interactions that predominantly occur at the focal volume. Light-induced refractive index variation governed by $\text{Re}[\chi^{(3)}]$ results in a detectable lensing effect. Two-photon absorption governed by $\text{Im}[\chi^{(3)}]$ removes photons from the probe beam, which is detectable and separable from the $\text{Re}[\chi^{(3)}]$ -related effect. Determination of $\chi^{(3)}$ of bulk and microcrystalline ZnO have been reported by using this technique [34]. However, the $\text{Im}[\chi^{(3)}]$ -related removal of photons in colloidal suspensions of ZnO NPs is superimposed on the elastic scattering exacerbated by often occurring NP aggregation (*cf.* data shown in Fig. 1) [31]. Besides, ZnO nanomaterial synthesis can yield low-concentration colloids whose $\text{Im}[\chi^{(3)}]$ -effect on the probe beam is difficult to detect. An alternative approach of measuring $\sigma_{\text{ZnO}}^{(2ph)}$ relies on counting PL photons versus controlled ZnO sample excitation parameters, where η_{ZnO} is determined separately [30]. The high sensitivity of this method is underpinned by the single-photon detection limit of modern photodetectors. Besides, $\sigma_{\text{ZnO}}^{(2ph)}$ measurement is

local, with ultimate sensitivity determined by the focused beam volume measured in sub-femtoliters.

In this paper, we report on a systematic study of ZnO NP nonlinear optical properties, with a two-fold aim: (1) addressing two characterization techniques suitable for determination of the two-photon action cross-section, and (2) establishing a numerical correspondence between the nonlinear optical microscopy signal of ZnO NP and nanoparticle distribution in skin, which paves a way for quantitative *in vivo* nanotoxicology studies.

2. Materials and method

2.1. Material description

Commercially available formulation Zinclear_60CCT (Antaria Ltd., WA, Australia) was used for characterization. The original formulation contained 60% ZnO NPs in organic solvent capric/caprylic triglyceride (CCT), in addition to poly-fatty acid, as the hyper-dispersant. Primary mean-size of ZnO nanoparticles was specified as 20 nm. The NPs were produced via mechanochemical technology, which allowed large-scale fabrication. Nanoscale ZnO was synthesized by milling and heat treatment of the mixture of ZnCl_2 , NaCl and Na_2CO_3 powders. Particle size was controlled by means of the reactant chemical ratio, milling time and heat treatment temperature. ZnO NP was then coated with stearic acid to render the surface hydrophobic to facilitate dispersion in silicone-based non-polar liquids, as in cosmetic formulations [35]. The resultant ZnO NPs were ellipsoidal in shape characterized by high crystal quality, as shown in Fig. 1.

2.2. Characterization

In order to determine physical properties of the as-received material, which contained ingredients used for topical application on human skin in cosmetic formulations and skin uptake experiments, size distribution of ZnO NP was measured by the dynamic light scattering method (DLS, Malvern Zetasizer ZS, UK) after dilution with original solvent CCT. Fluorometer (Fluorolog Tau3 system, JY Horiba) was employed to measure the photoluminescence (PL) spectra of ZnO NP. Due to the intrinsic fluorescence of CCT, ZnO NPs were subsequently extracted from CCT and distilled in deionized water (DDW). ZnO NP absorption spectra were measured using UV/Vis spectrometer (Carry 5000, Varian). In order to minimize the scattering effect, the suspension was placed in a 2-mm pathway high-grade UV quartz cuvette. In the concentration range of our study, the scattering mean-path is much greater than the pathway of the cuvette, so it can be regarded as a single scattering event. Besides, the scattering cross-section of ZnO NPs was small compared with the absorption cross-section, and can be neglected. The sample PL quantum yield was determined by comparison of the linear (as opposed to nonlinear) emission to absorption ratio with respect to that of tabulated organic fluorescence dye, Stilbene 1, using controlled concentration of both samples, as detailed in Results.

Primary size of ZnO NPs was determined by using transmission electron microscopy (TEM). ZnO NPs were extracted from the Zinclear_60CCT in acetone, then dried out on a clean glass slide. The collected powder was redispersed in ethanol at a concentration of 0.01 - 0.1 mM (defined in terms of the ZnO crystal unit cell), and imaged using TEM (Philips CM10).

ZnO NP hydrodynamic mean-diameter (yielding ~10% overestimate of its physical size) was determined via DLS by using 0.1-mM and 1-mM solutions in various solvents, including DDW, ethanol, methanol, acetone, and CCT. 15-min sonication of the samples was carried out prior to these measurements.

We used two methods to evaluate the two-photon absorption cross-section of ZnO NP. Method 1 was an absolute measurement developed by Kauert *et al.*, which involved a flow cell and a TPSPC measurement module (Becker and Hickl) [36]. The wavelength was fixed to

795 nm. The second method was based on the integral measurement of a thin ZnO NP layer nonlinear optical signal using the nonlinear optical microscopy setup. The wavelength-tunable femtosecond laser in NLOM system was set to 770 nm to attain the maximum contrast ratio of ZnO NP signal versus skin autofluorescence, as detailed in Subsection 3.3.

2.3. PVA nanoscale thin film fabrication

For the NLOM-based determination of $\eta_{\text{ZnO}}\sigma_{\text{ZnO}}^{(2ph)}$, it was essential to prepare a film with uniform distribution ZnO NPs. Spin-coating method was employed, with polyvinyl alcohol (PVA), as a host polymer. By mixing 10% PVA w/w water solution with pre-dispersed ZnO NP solutions 1:1 volume ratio, films of various ZnO concentrations were fabricated. A 90-nm thin film was deposited on a coverslip (thickness, 170 μm) by spin-coating PVA for 1 min at a speed of 8000 rpm, followed by drying in an oven at 40°C overnight allowing 99% of the solvent (water) to be evaporated. The surface smoothness and the degree of homogeneity were evaluated by a scanning electron microscope (SEM, JEOL 6480 LA). The film thickness was determined by an optical profiler (WYKO NT 3000) via measuring a step profile at the interface of film-glass substrate.

2.4. Skin sample preparation

Human skin patches were excised from, predominantly, female donors aged between 30 and 40 years ($n = 3$) who had undergone abdominoplasty surgery. All experiments conducted on human subjects were carried out with the approval of Princess Alexandra Hospital Human Ethics Research Committee (Approval no. 097/090, administrated by the University of Queensland Human Ethics Committee), and the subjects gave their written consents. 10 μL of the 60% w/w Zinclear formulation in the CCT solvent was applied on the 1.33 cm^2 skin human skin patches, which were fixed in a standard Franz cell and incubated at a 37°C-warm water bath. The application dose was slightly higher than that recommended for daily application (2 mg/cm^2) according to the Food and Drug Administration (FDA) and the international protocols. The formulation was massaged into the skin surface for 5 min, prior to incubation at 37°C, and washed off after 8 hours of incubation.

The treated human skin samples were encased in polyether wax and cut into 8- μm -thin cross-section slices followed by sandwiching between standard microscopy glass slides and coverslips, which were ready for NLOM imaging.

2.5. Microscopy

Experiment configuration

A nonlinear optical microscopy system (Leica DM IRBE/TCS SP2) was employed for imaging of the ZnO NP-treated human skin samples. A tunable titanium-sapphire femtosecond-pulsed laser (Tsunami, Spectra Physics), pumped by a 5-Watt CW laser (Millennia, Spectra Physics) was employed, as the excitation source. The laser wavelength was set to 770 nm. The laser pulse width was evaluated as < 150 fs, at a repetition rate of 80 MHz, the spectral bandwidth was measured to be ~10 nm, average power at the sample, 70 mW. The laser beam was focused in the sample by a high-NA, oil-immersion microscope objective (40 \times , NA 1.3).

TPIL-signal excited by the laser was collected by the objective lens and passed through a filter cube that comprised a 700-nm short-pass filter to block the excitation at 770 nm, followed by a bandpass dichroic mirror 390 ± 40 nm. The filtered UV-emission of ZnO NP was detected by using a photomultiplier tube; while two-photon-induced autofluorescence signals of the skin tissue (broad emission centered at 550 nm) was suppressed [23].

An UV diode laser (405 nm) excitation was employed to acquire skin morphology by collecting autofluorescence signal of the skin endogenous fluorophores, such as NAD(P)H, flavins, collagen, elastin, and melanin (the filter cube filter was tuned to a spectral band of

420–500 nm). The skin autofluorescence and TPIL images were color-coded green and red, respectively, and overlaid to display ZnO NP distribution in skin. The quantitative imaging will be interpreted in more detail in the Results and discussion Subsection 3.4.

The acquired images were processed by Igor Pro (Wavemetrics) software. SC was manually delineated in each image allowing a purpose-designed software code to calculate the direction normal to the skins surface at each point. This was used to flatten the skin surface along one axis (*x*-axis), while setting a perpendicular *y*-axis along the in-depth direction in skin. The sum of the *y*-profiles were averaged over every TPIL image, and over all images to obtain the ZnO NP distribution in-depth profile, while the autofluorescence signals were averaged using the same algorithm to produce the skin profile.

3. Results and discussion

3.1. Size determination

The Zincclear₆₀CCT size dispersion was determined in the as-received organic solvent of caprylic capric triglyceride (Sample 1), and in either water, or alcohol, or acetone (Sample 2). Sample 1 was well-dispersed and stable due to its hydrophobic surface coating, which rendered NPs water-repellent and dispersible in non-polar organic solvents, such as CCT. In addition, the surface coating modified the chemical stability and decreased the photocatalysis by surface passivation. Figure 2 shows reasonably monodisperse size distribution of Sample 1 (mean hydrodynamic diameter, 35 nm, FWHM 15 nm) measured by DLS in the diluted original CCT solution. A subtle peak in the size-range of 60 - 120 nm was an indication of the aggregation, which was removable by sonication. Sample 2 exhibited aggregation, which was

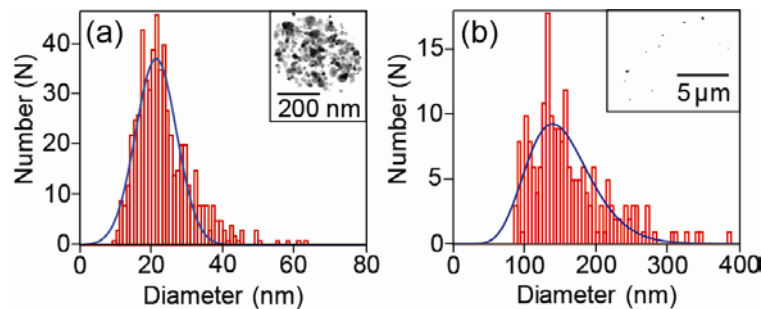


Fig. 1. A high-magnification TEM image of the well-dispersed ZnO NPs (Sample 1) displaying single particles (left inset); and ZnO grain size histogram (left panel). A low-magnification TEM image of Sample 2 (right inset), with a size distribution histogram showing NP aggregations (right panel). Solid (blue) line represent the size distribution fit to a Gaussian function used to determine the distribution mean-size and standard deviation.

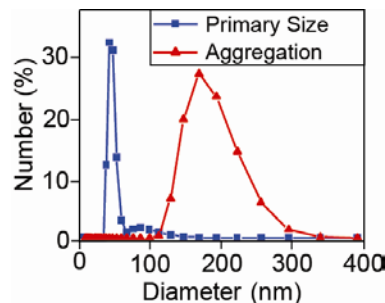


Fig. 2. Size distribution of the Zincclear (ZnO NP) sample measured by DLS: Sample 1, as-received ZnO NPs in CCT organic solvent, square symbol; the blue line, represents a distribution of primary sizes. Sample 2, redispersed in acetone, triangle symbol; the red line represents an agglomerated state.

due to the ZnO NP surface hydrophobic and charge properties. Despite aggregation, NPs retained their granularity, as observable in TEM images (Fig. 1(a)). The aggregate size distribution was consistent and relatively narrow, 160 ± 30 nm (Fig. 2, red curve). Note that the hydrodynamic diameter provides an approximately 10% size overestimate of the physical diameter, as measured by TEM (Fig. 1, insets).

TEM afforded accurate sizing of the Samples. High-magnification TEM images were captured to examine the granular content of the Sample 1, which was statistically analyzed to produce a size distribution histogram, as shown in Fig. 1(a). Low-magnification TEM images captured aggregation size properties of Sample 2. Figure 1(b) shows a representative image, with the aggregation mean-size of 150 nm corroborating the DLS measurement results.

3.2. Linear spectral properties of ZnO NP

Photoluminescence quantum yield (η) is an important parameter of an emitter defined as a percentage value of the emitted photon energy per one absorbed photon energy. η of ZnO NP was determined by comparing emission/absorption ratio of Sample 2 of the molar concentration (in terms of ZnO unit cells) 1 mM to that of the organic fluorescence dye Stilbene 1 (Sb1). Sb1 concentration was maintained at 0.05 mM throughout all measurements as a trade-off between maximized fluorescence signal and onset of the self-quenching effects. A representative absorbance [defined as $-\log_{10}(I_t/I_0)$, where I_0 and I_t are incident and transmitted intensities, respectively] spectra of the 1-mM Sample 2 and 0.05-mM Sb1 are shown in Fig. 3. The spectrum of ZnO NP is characterized by a strong absorption in an UV band extending considerably into the UV-range, with a local absorption peak at 362 nm, whereas Sb1 absorption is characterized by a relatively narrower spectral band centered at 350 nm. Peak absorbances of Sample 2 and Sb1 were measured to be 1.34 and 1.27, respectively (Fig. 3).

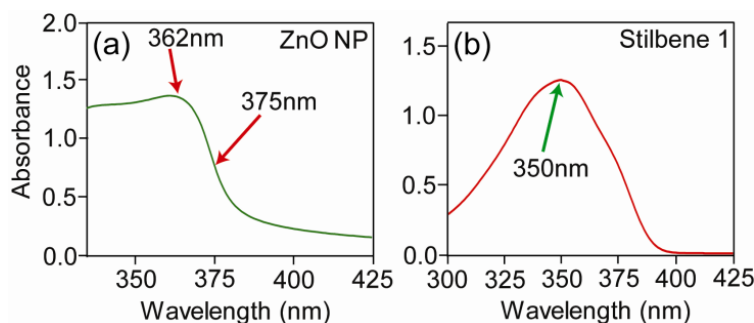


Fig. 3. (a) Absorption spectrum of 1-mM Zinclear_60CCT, Sample 2, redispersed in acetone; (b) absorbance spectrum of 0.05-mM Sb1 dissolved in ethylene glycol.

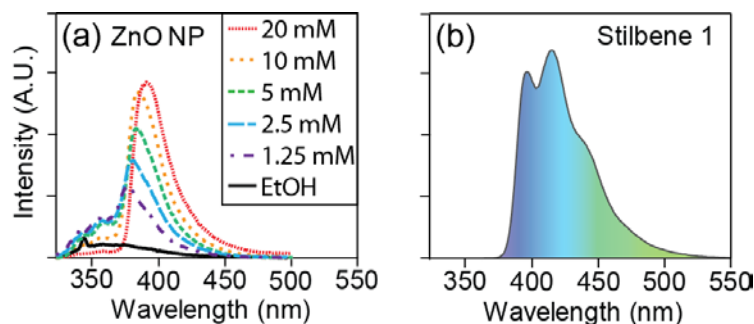


Fig. 4. Emission spectra of (a) ZnO-NP (varied concentration, excitation wavelength, 310 nm), The pure ethanol emission spectrum was used, as a baseline (solid black line); and (b) Stilbene 1 (0.05 mM, solvent, ethylene glycol), excitation wavelength, 350 nm.

Emission spectra of Sample 2 redispersed in ethanol in variable concentrations were compared with these of Sb1, excited at 350 nm to achieve maximum quantum efficiency (Fig. 4). The concentration-dependent red-shift of the ZnO-NP emission peak was attributed to the self-absorption.

In order to determine the quantum yield of the ZnO NP sample, η_{ZnO} , one needs to ratio emitted to absorbed intensities, respectively. The absorbed intensity is determined in terms of absorbance by using the Beer-Lambert law:

$$A = -\log_{10}(I/I_0) = (\log_{10} e) \varepsilon l C_M, \quad (1)$$

where A is the measured absorbance, ε [$\text{cm}^{-1} \cdot \text{M}^{-1}$] is the molar absorptivity of the sample, l is the pathway length, and C_M [M, or mol/L] is the molar concentration. The emitted PL power is determined as

$$P = \xi \eta \varepsilon C_M \langle I \rangle, \quad (2)$$

where $\langle I \rangle$ is the averaged excitation intensity taking into account the beam attenuation in the sample; ξ - collection efficiency, which is an instrumentation parameter, assumed equal for both ZnO NP and Sb1 samples. By relating the emitted power of ZnO NP to that of the Sb1 sample, integrated over the equal spectral bands, one finds a quantum yield ratio given by

$$\frac{P_{\text{ZnO}}}{P_{\text{Sb1}}} = \frac{\eta_{\text{ZnO}}}{\eta_{\text{Sb1}}} \frac{A_{\text{ZnO}}}{A_{\text{Sb1}}}. \quad (3)$$

η_{Sb1} was reported to be 0.56, allowing straightforward calculation of the percentage value of $\eta_{\text{ZnO}} = (0.9 \pm 0.2)\%$. This value is comparable with the reported values [10,37].

3.3. Two-photon action cross-section

The first method for determining the two-photon action cross-section of ZnO, $\eta_{\text{ZnO}} \sigma_{\text{ZnO}}^{(2ph)}$ has been described in detail by Kauert *et al.* [36]. Briefly, ZnO NP suspension was injected into a flow cell and illuminated by a focused, 795-nm ultrashort-pulse laser system (Mira 900 pumped by Verdi V10, Coherent) of the pulse width of 130 fs and average power ranging from 3 to 30 mW, with an TPIL signal being recorded versus the illumination (excitation) power. Rhodamine 6G (Rh:6G) dissolved in ethanol was used, as the calibration standard. The method ability to count single TPIL events allowed accurate determination of the detected fluorescence or PL power, i.e. either a single Rh:6G molecule, or a well-defined single aggregate of ZnO NP. Also, this method afforded the substantial excitation laser power, as the photo-degraded molecules/NPs in the flow were quickly replenished. In addition, the single-photon counting technique allowed measurement of the TPIL decay time by using a TPSPC measurement module. An example of the TPIL single-photon correlation dependence that related to PL time trajectory is shown in Fig. 5(a). The ZnO NP decay curve was fitted by two exponentials, with a short component of $\tau_1 = 139$ ps, associated with emission in the UV/blue spectral band, and a long component, $\tau_2 = 3.1$ ns, associated with ZnO NP emission in the green spectral band. The green emission is commonly attributed to oxygen-defects in the bulk crystal and/or oxygen surface defects [27]. The longer TPIL decay component reported by the others was not detectable using our set up [12]. Figure 5(b) shows a log-log plot of the emission intensity versus the incident power. The slope of the fitted line is $\cong 2$, which indicated that the two-photon absorption process played a major role [25].

The two-photon action cross-section was calculated by using the following formula [36]:

$$\eta_{\text{ZnO}} \sigma_{\text{ZnO}}^{(TPIL)} = \frac{TPIL_{\text{ZnO}} C_{\text{Rh}} \eta_{\text{Rh}} \sigma_{\text{Rh}}^{(2ph)}}{TPIL_{\text{Rh}} C_{\text{ZnO}}}, \quad (4)$$

where C represents number concentration of the samples (samples are denoted by subscripts Rh, ZnO for Rh:6G and Zinclear ZnO NP samples, respectively); TPIL stands for the detected signals. We note that the two-photon action cross-section of an agglomerate (demarcated by an asterisk in the subscript) was determined. It was recalculated as $\eta_{\text{ZnO}}\sigma_{\text{ZnO}}^{(2ph)}$ for a single crystal unit cell of ZnO to be $6.2 \pm 0.8 \mu\text{GM}$, using ZnO density of 5.6 g/cm^3 and molecular weight of 81.41 g/mole . The single crystal unit cell was defined to contain one pair of Zn and O ion (ZnO dimer) for the purpose of comparison convenience.

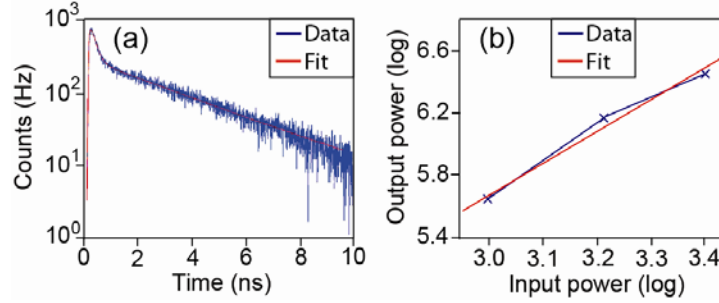


Fig. 5. (a) Time-resolved single-photon correlation signal of ZnO NP showing fast and slow decay components. Data fit, red line. (b) Log-log plot of the power dependence of ZnO NP on a scale (\times , blue line). The data is linear-fit (solid red line), with a fitted slope of 2.

It was straightforward to evaluate the two-photon action cross-section of 1.19 GM per primary particle of 20.6 nm in size estimating $N_{u.c.} = 1.9 \times 10^5$ unit cells per particle. While aggregation was present in the solution, the optical absorption from the ZnO was small. It is worthwhile to provide $N_{u.c.}\eta_{\text{ZnO}}\sigma_{\text{ZnO}}^{(2ph)}$ per single primary particle for comparison with the other reported values, where the aggregation was not considered. Also, Zinclear formulation represented a well-dispersed suspension of the primary particles in CCT oil, largely retaining its quasi-monodispersity, when applied topically on human skin [12], so that the detected TPIL signal should be linearly related to $N_{u.c.}\eta_{\text{ZnO}}\sigma_{\text{ZnO}}^{(2ph)}$ providing a direct primary particle distribution read out in human skin.

The second method used to determine $\sigma_{\text{ZnO}}^{(2ph)}$ was based on the calibrated-throughput nonlinear optical microscopy. The simplicity of this method was appealing, but traded off by the potential accuracy inferior to that of the first method. Thin PVA films (thickness, 90 nm) of Sb1 and ZnO NP at various concentrations were NLOM-imaged, multiple images were acquired for each concentration, and the average intensity over all images was calculated. The microscope operation parameters were maintained constant during the image acquisition, except that the twice greater femtosecond laser power was used to illuminate the ZnO NP samples in comparison with the Sb1 samples. To remove artifacts arising from fluctuations in the microscope system and detector photoresponsivity for each image, a second image was acquired, with the laser switched off, referred to as the background, B , and its average value was subtracted from the initial image (signal, S).

The resultant TPIL signal was averaged over the ZnO-NP/PVA-film sample field of view, to minimize the effects of the ZnO NP aggregation, assuming that the self-absorption effect remained negligible in the 90-nm -thin film. Scanning electron microscopy (SEM) of the ZnO-NP/PVA-film confirmed that a quasi-single layer of particles was observable and their sub-micron features were discernable. $\sigma_{\text{ZnO}}^{(2ph)}$ was calculated by using the following equation:

$$S - B = \xi \eta_{\text{ZnO}} \sigma_{\text{ZnO}}^{(2ph)} C_N I^2, \quad (5)$$

with all the variables defined previously. In order to eliminate the poorly controllable collection efficiency parameter, ξ from Eq. (5), one needed to benchmark the ZnO TPIL signal against that of the tabulated fluorophore, such as Sb1. $S-B$ vs. C_N data were acquired experimentally and graphed in Fig. 6. An TPIL signal slope of Sb1, defined as $Slope = (S-B)/C_N$ was determined to be 3.4×10^6 arb. un. (arbitrary units) using the data plotted in Fig. 6(b). The reported value of two-photon absorption cross-section of Sb1 is $12.1 \times 10^{-50} \text{ m}^4/\text{s/photon.particle}$ (12.1 GM), with the quantum yield of 0.56 [38].

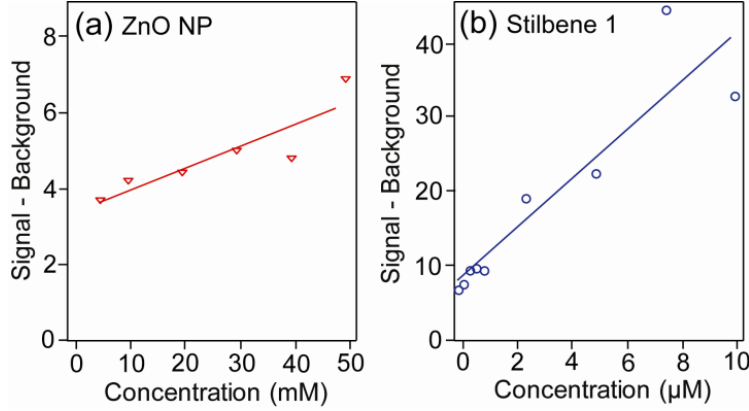


Fig. 6. TPIL emission signal versus concentration of: (a) ZnO and (b) Sb1. The data were fitted with straight lines. For ZnO NP, the signal saturated at the higher concentrations, due to the self-absorption, the lower limit was set by the detection sensitivity.

The TPIL signal slope of ZnO NP is given by

$$Slope_{ZnO} = 4\xi\eta_{ZnO}\sigma_{ZnO}^{(2ph)}I^2, \quad (6)$$

Since the two-photon action cross-section is linearly proportional to the two-photon absorption cross-section, with a proportionality constant being the quantum efficiency of the emitter, the quantum efficiency was assumed invariant over the process order and spectral range [39]. With $\eta_{ZnO} = 9 \times 10^{-3}$, as described in 3.2, and the factor of 4 accounting for the twice greater excitation power in comparison with that of Sb1. $Slope_{ZnO}$ was determined to be 55.3 arb. un. using the data plotted in Fig. 6(a) that yielded $\sigma_{ZnO}^{(2ph)} = 4 \text{ mGM}$ and $\eta_{ZnO}\sigma_{ZnO}^{(2ph)} = 32 \pm 6 \text{ } \mu\text{GM}$ per ZnO dimer, which corresponded to $N_{u.c.}\sigma_{ZnO}^{(2ph)} = 700 \text{ GM}$ and $N_{u.c.}\eta_{ZnO}\sigma_{ZnO}^{(2ph)} = 6 \text{ GM}$ per a primary particle. The estimated error of 25% was due to the non-reproducibility of the sample preparation procedure and uncontrollable detection parameters, such as the femtosecond laser pulsewidth, estimated using the assumption of the Fourier-limited transform of the spectral bandwidth.

A reasonable agreement was found between the two different presented methods, with the discrepancy attributed to the different excitation wavelengths. The excitation centered at 770 nm, was effectively on the falling slope of the ZnO NP excitation curve (*cf.* Figure 3(a) at 385 nm), whereas the excitation centered at 795 nm, was well outside of the ZnO NP excitation band. The excitation of ZnO NP still took place due to the finite spectral bandwidth (FWHM $\sim 10 \text{ nm}$) of the femtosecond laser in both methods, but the excitation efficiency was apparently greater at 770 nm, which was reflected in the corresponding values of $\sigma_{ZnO}^{(2ph)}$. Comparison with the previously reported results shows that $\sigma_{ZnO}^{(2ph)}$ per unit cell of the investigated ZnO NP sample, Zinclear is an order of magnitude greater than $\sigma_{ZnO}^{(2ph)}$ recalculated from the measured value of $Im[\chi^{(3)}]$ of ZnO NP at the excitation wavelength of

532 nm [30]. We speculate that the mechanochemical synthesis provided a considerably better crystal quality of ZnO NPs evidenced by very little PL in the green spectral band (*cf.* Figure 4(a)) than that of the sol-gel method used in Ref. [25]. Also, the excitation spectral band at 532 nm in comparison with that of 770 nm was irrelevant to NLOM-based studies biomedical studies. We also note that the determined ZnO NP two-photon action cross-section, 6 GM, was markedly higher than that of the skin-dominant endogenous fluorophores, < 0.1 GM at 700 nm [40], thus explaining the high-contrast images of ZnO NP/skin obtained in Ref. [10].

The conventional nonlinear optical microscopy appeared to be capable of determining the nonlinear properties of optical nanomaterials. By knowing $\eta_{\text{ZnO}} \sigma_{\text{ZnO}}^{(2ph)}$, one can determine ZnO nanoparticle concentration in (biological) samples by using TPIL signals, as demonstrated in the final subsection.

3.4. Quantitative assessment of ZnO NP uptake in skin

Using the calibrated NLOM system, as detailed above, the tissue slices of ZnO-NP-treated skin were imaged. ZnO NP concentration was measured in terms of particles per cubic micron by using Eq. (5) and the calibration curve of ZnO NP versus pixel signal intensity on image. Using our developed quantitative imaging method, distribution of ZnO NPs in the epidermis of the excised human skin sample was assessed. An in-house developed algorithm was used to process the NLOM cross-sectional images, as shown in Fig. 7(a), such that the skin surface was unfolded into a straight line lending accurate determination of the ZnO NP distribution in epidermis, as plotted in Fig. 7(b). Figure 7(a) shows a cross-section morphology of the skin sample rendered visible by the autofluorescence excited by a 405-nm laser, detected in the visible spectral band, and color-coded green. One can observe (left to right) dermis layer, bright-green viable epidermis layer populated by cells, with discernible dark round nuclei, and a faint layer of SC, with a white contour roughly outlining the sample boundary. TPIL ZnO NP signals are color-coded red, and observable in SC, especially, two conspicuous clusters, but not in viable epidermis. Some traces of red color-coded signals in the dermis layer were attributed to SHG signals from the collagen fibers.

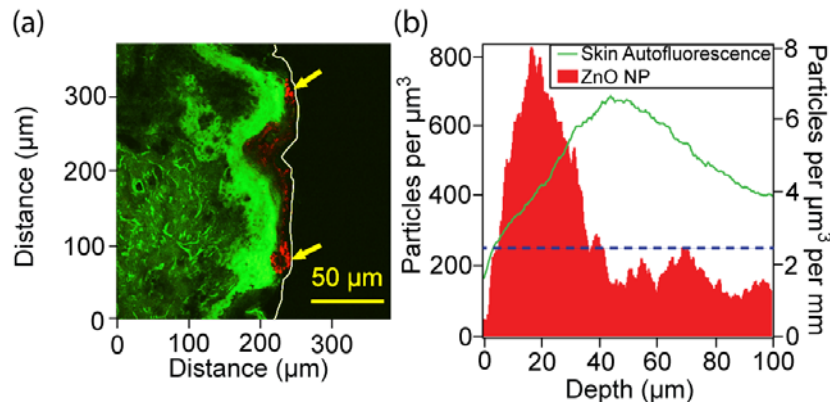


Fig. 7. (a) An overlay of the confocal/multiphoton image of the excised human skin, and (b) plot of the ZnO NP distribution versus the skin depth processed from the image data. Left panel: green color, skin autofluorescence excited by 405 nm; red color, ZnO NP distribution in skin (*stratum corneum*) excited by 770 nm, with collagen-induced faint SHG signals in the dermal layer. Yellow arrows point to ZnO NP clusters. Right panel: ZnO NP concentration in the epidermis. A threshold line (dashed, blue) delineates spurious signals due to the image processing artifacts (below the line) from the ZnO NP signals. The right-hand-side axis, ZnO NP concentration per unit length averaged across the entire imaged skin surface.

It was found that the 21-nm primary-size ZnO NPs exhibited small absorption in *stratum corneum*, with no detectable absorption in viable epidermis, which was consistent with the

existing body of evidence [10]. We found that ZnO NPs were primarily situated in SC, with occasional protrusion to the areas of dermatoglyphs (skin folds). Figure 7(b) shows an averaged skin autofluorescence profile (green solid line) plotted together with ZnO NP signal (red area graph). The autofluorescence profile maximum demarcates the onset of the viable epidermis, which fades away slowly toward the deeper skin layers. Firstly, this data allowed direct assessment of the ZnO NP absorption in skin, where the signal was seen to be accumulated on the surface and in SC, possibly, in dermatoglyphs. Secondly, and most importantly, direct read-out of ZnO NP concentration was obtained reaching about 800 particles per μm^3 at the depth of the conspicuous cluster localization. The right-hand y-axis of this plot also provided a quantitative read-out of the ZnO NP concentration per sample unit length, as averaged over the entire skin tissue sample.

4. Conclusion

We investigated the physical and optical properties of typical commercial ZnO NPs, Zinclear. In the organic solvent, ZnO NPs remained dispersed, with a mean diameter of 21 nm, whereas in polar solvents, e.g. water, alcohol, the nanoparticles were gradually aggregated to a mean-diameter of ~ 200 nm. Characterization of the sample optical properties yielded a photoluminescence quantum yield of $(0.9 \pm 0.2)\%$. A two-photon action cross-section measured by the two nonlinear optical microscopy based methods, provided $6.2 \pm 0.8 \mu\text{GM}$ at 795 nm, and $32 \pm 6 \mu\text{GM}$ at 770 nm, which was considerably greater than the values of the dominant endogenous fluorophores in biological tissue.

We have also demonstrated a method of quantitative assessment of ZnO NP distribution profile in human skin suitable for non-invasive measurements *in vivo*. ZnO NP distribution peaking at the concentration value of 800 particles per μm^3 was located at the topmost layer of skin, *stratum corneum* and in skin folds, with no detectable signal in viable epidermis. The reported investigations are believed to be enabling for *in vivo* nanotoxicology studies considering the granted ethic clearance for ZnO-formulations.

Acknowledgment

One of us (Z. S.) wishes to acknowledge Macquarie University postgraduate research funding supporting this work.